

Three-dimensional impurity transport modeling of neon-seeded and nitrogen-seeded LHD plasmas

journal or publication title	Plasma Physics and Controlled Fusion
volume	60
number	8
page range	084005
year	2018-06-19
URL	http://hdl.handle.net/10655/00012664

doi: 10.1088/1361-6587/aac9ea



Three-dimensional impurity transport modeling of neon-seeded and nitrogen-seeded LHD plasmas

G. Kawamura^{1,2}, H. Tanaka³, K. Mukai^{1,2}, B. Peterson^{1,2}, S. Y. Dai⁴, S. Masuzaki^{1,2}, M. Kobayashi^{1,2}, Y. Suzuki^{1,2}, Y. Feng⁵, and LHD Experiment Group¹

¹National Institute for Fusion Science, National Institutes of Natural Sciences, Toki 509-5292, Japan

²Department of Fusion Science, Graduate University for Advanced Studies (SOKENDAI), Toki 509-5292, Japan

³Graduate School of Engineering, Nagoya University, Nagoya 464-8603, Japan

⁴Key Laboratory of Materials Modification by Laser, Ion and Electron Beams (Ministry of Education), School of Physics, Dalian University of Technology, Dalian 116024, People's Republic of China

⁵Max-Planck-Institut für Plasmaphysik, D-17491 Greifswald, Germany

E-mail: kawamura.gakushi@nifs.ac.jp

December 2017

Abstract. Modeling of impurity-seeded plasma in Large Helical Device (LHD) is presented for the first time by using the three-dimensional transport code EMC3-EIRENE. High and low recycling coefficients for impurity ions are assumed to include low and high absorption rates on wall surfaces due to low and high chemical activity of neon and nitrogen, respectively. Radiation power measured by two bolometer systems and particle flux measured by divertor probes installed in multiple toroidal sections are utilized to determine impurity amount in the plasma. The toroidal uniformity and the non-uniformity of a divertor flux reduction observed experimentally for neon and nitrogen seeding, respectively, are reproduced by the model. Validations by measurements and deviations between the model and the experiment are discussed.

PACS numbers: 52.25.Vy, 52.25.Xz, 52.25.Ya, 52.55.Hc, 52.65.Kj

Keywords: EMC3-EIRENE, modeling, divertor plasma, impurity seeding

1. Introduction

Modeling of a fusion plasma is one of the urgent tasks for an engineering design of a reactor-class device. Reliable estimation of plasma parameters such as electron density and temperature in a certain device and with a certain discharge condition should be realized through development of models for existing devices including tokamak, helical, and linear devices. Prediction of a plasma is essential for a reactor design to ensure safety

margins to engineering limits and good controllability of discharges. Increase of core performance, enlargement of device size, and extension of discharge time leads to severe engineering issues such as high heat load on the plasma facing components statically or dynamically [1, 2] and accumulation of impurities and hydrogen isotopes on wall surfaces[3, 4]. These issues are closely linked to divertor plasma transport. Therefore, the modeling of divertor plasma is strongly required to estimate the plasma parameters and the influence upon components surrounding the plasma. In particular, regarding the heat load issue, application of impurity radiation[5, 2], optimization of divertor structure[6, 7], and plasma detachment[8, 2] are the major topics.

Divertor plasma modeling of fusion devices is studied with calculation codes solving fluid equations of plasma along magnetic field lines terms and kinetic equations of neutral particles. Codes for tokamak devices assume axisymmetry, however plasmas with Resonant Magnetic Perturbations (RMP) in tokamak devices and plasmas in helical devices require a three dimensional calculation code. EMC3-EIRENE code[9, 10, 11] is a three dimensional Monte Carlo code extensively applied to fusion devices with non-axisymmetric components. Fluid transport equations along the magnetic field with perpendicular diffusive transport are solved by EMC3 code, and kinetic transport equations with atomic and molecular processes are solved by EIRENE code. The coupled code has been applied to Large Helical Device (LHD)[12], and many modeling studies have been conducted[13]. The calculation region has been extended to the whole plasma including divertor legs[14], and impurity transport modelings have been conducted[15].

Impurity seeding experiments with gas puffing have been conducted[16, 17] with different gas species, such as neon, argon, krypton, xenon, and nitrogen. Recently, an experimental analysis with regard to toroidally symmetric/asymmetric distributions of particle flux on divertor plates was carried out[18]. As a result, differences of transport characteristics of neon and nitrogen were revealed in LHD. A helical plasma intrinsically has a toroidal asymmetry. However, the helical plasma usually has a toroidal periodicity due to repeated toroidal structures of magnetic field coils. We note that a toroidal symmetry in this work represents the periodicity, and a toroidal asymmetry represents violation of the periodicity. In this work, we present a modeling study of impurity-seeded plasma with EMC3-EIRENE code to reproduce the toroidal symmetric/asymmetric characteristics. Also, validation of the model with experimental measurements and open questions suggested from differences between model results and experimental measurements are addressed.

In this paper, the transport model in the code, modeling of impurity recycling, impurity source, and the device configuration are described in Secs. 2.1, 2.2, 2.3, and 2.4, respectively. After an explanation of discharge conditions and modeling parameters for simulating plasma with such discharge conditions in Sec. 3.1, calculation results and discussion of neon and nitrogen seeding are presented in Secs. 3.2 and 3.3, respectively. Finally, the summary is given in Sec. 4.

2. Modeling of impurity seeding

2.1. Transport and atomic processes

We employed EMC3-EIRENE code[9, 10, 11, 13, 14, 15, 19] to model impurity-seeded plasmas in LHD and to obtain distributions of various physical quantities in steady state. The code describes a plasma with Braginskii-type two fluid equations along magnetic field lines with cross-field diffusion and neutrals with a Boltzmann-type kinetic equation with atomic and molecular processes. The cross-field diffusion coefficients D_{\perp} , $D_{\text{imp}\perp}$, $\chi_{e\perp}$, and $\chi_{i\perp}$ for hydrogen plasma, impurity ion, electron energy, and ion energy, respectively, can be given by functions of position[9, 19] in order to model anomalous transport. In this work, we use spatially uniform values for these coefficients. The code can solve the plasma in an ergodic region, a Scrape-Off Layer (SOL), and a divertor region. A core region is excluded, but it is modeled as boundary conditions. Particle drifts are not modeled in the code. The toroidal resolution of the EMC3-EIRENE grid is 0.25° . Multiple cells defined by the grid are combined into a larger cell except near the divertor plates in order to reduce the computational cost.

Hydrogen, deuterium, or tritium can be solved as the main plasma species with particle, momentum, and electron/ion energy equations[10]. In this work, we use hydrogen as a main plasma component. Each charge state of impurity species is solved with particle and momentum equations under the assumption of the equal temperature with the main plasma ion. The code does not include electron source from impurities, but it does include energy interactions between the impurity and the electron in the main plasma due to ionization, recombination, and radiation. We used ADAS database[20] for impurity atomic processes and TRIM database [21, 22] for Plasma-Surface-Interaction processes of hydrogen, e.g., reflections with energy loss and recombination from atoms to molecules. The surface process for impurity neutrals is modeled as a mirror reflection with a reflection coefficient.

2.2. Recycling of impurity

Difference in transport property with regard to impurity species has been investigated in experiment studies. In LHD, different time scale and toroidal asymmetry are obtained from gas-puffing experiments using neon and nitrogen. Increase of radiation, increase of electron density in divertor regions, and decrease of electron temperature are commonly observed during and/or after a puff[16]. However, decay time of these influences depends on the impurity species. A typical decay time of radiation from neon is a few seconds. On the other hand, a typical decay time of radiation from nitrogen is less than one second. These time scales are much longer than the transport time scale of plasma and, therefore, other physical processes outside the plasma are suggested with regard to the decay time. Higher loss rate of impurity gas on wall surfaces causes shorter decay time of radiation. Impacts of loss of impurity gas are discussed based on experiment observations in this section.

Difference in a toroidal distribution with regard to impurity species is observed in experiments. Nitrogen radiation observed by a bolometer at a certain toroidal section is much weaker than neon radiation observed by the same bolometer even when a similar magnitude of influence is observed in an upstream plasma near the Last Closed Flux Surface (LCFS). That implies different transport characteristics caused by different atomic and molecular processes, different ionization energy, different plasma-surface interactions between neon and nitrogen. A direct measurement of an asymmetric reduction of particle flux has been reported[18]. A flux reduction on divertor tiles is almost toroidally symmetric in the case of a neon puff and clearly asymmetric in the case of a nitrogen puff. That implies that neon-seeded plasmas lose connection with the source position of the puff, but nitrogen-seeded plasmas maintain connection with the source position.

From the above observations, the difference between neon and nitrogen is considered to arise from the neutral loss of impurity on the wall surfaces. Experimental studies suggest that neon concentration seems small in carbon[23] and in stainless steel in LHD[24]. On the other hand, nitrogen concentration seems significant in carbon[25] and in tungsten in ASDEX Upgrade[26]. The large retention of nitrogen is considered to be a result of high chemical activity.

In this study, impurity transport of seeded neon and nitrogen has been modeled by 100% and by 0% recycling coefficients at the divertor plates, respectively. The two recycling coefficients correspond to high and to low absorption rates due to low and high chemical activity of neon and nitrogen, respectively. Although the zero recycling is an extreme condition, we chose the recycling coefficients to observe their influence clearly. In an experimental study[27], a small recycling coefficient of nitrogen, ≈ 0.3 , has been reported in Alcator C-Mod. In order to realize the recycling of impurity at the divertor plates, we extended the code to calculate the impurity ion flux on the surface and to use the flux to determine the impurity atom flux released from the surface. The modified version of EMC3-EIRENE has a switch for choosing one of the two impurity source distribution models, i.e., sputtering due to the hydrogen ion flux and recycling due to the impurity ion flux. The sputtering source uses the flux distribution of hydrogen ion on the divertor plates in the same manner as the original EMC3-EIRENE code. We note that physical sputtering by impurities is not implemented. The impurity recycling source uses the flux distribution of impurity ion itself on the divertor plates. The two source models are exclusive.

2.3. Source and sink

In addition to the coefficients described above, source and sink are essential parameters to determine transport. Neutral particles are generated or removed by gas release from plasma-facing surfaces, gas exhaust on pumping surfaces, and external neutral sources such as gas puffing nozzles. Ion and electron particles are injected or removed by volume sources due to ionization of hydrogen neutrals, external surface sources from

boundaries facing a core plasma, surface recombination sinks on plasma-facing surfaces, and surface sinks at a boundary between a plasma region and a vacuum region. These four sources/sinks should be always balanced in a steady state from a physical point of view. However, some adjustments must be considered in the model in order to compensate for the external factors and the loss components arising from numerical conditions such as plasma-vacuum boundaries. The EMC3-EIRENE code adjusts the neutral gas flux release from the divertor plates to realize a particle balance. The adjustment implies an imbalance of particle flux in the surface recombination process and causes pumping or puffing of gas on the surfaces practically. The amount of the adjustment is typically ignorable compared with the ion flux or the neutral flux if there are no large pumps or external sources. In EMC3-EIRENE code, ion flux to the plasma-facing surfaces is called “recycling flux” and is used to determine or control global particle source.

Energy is injected from the core boundaries and from external volume sources for plasma heating, and is removed on plasma-vacuum boundaries, on plasma-facing surfaces, and by atomic processes. The energy sink on plasma-vacuum boundaries is a perpendicular loss determined by cross-field transport coefficient and a decay length is given by an input parameter. The energy sink on the plasma-facing surfaces is a parallel loss determined by sheath heat transmission factors. The atomic processes include ionization and radiation with electron energy loss and charge exchange with ion energy loss.

In this study, external gas puffing is not used for hydrogen and external ion source from the core boundary is used to model particle deposition due to Neutral Beam Injection (NBI) heating, which is estimated by an effective heating power divided by the beam energy. The particle loss from the plasma-vacuum boundaries is much smaller than the recycling flux, typically $< 1\%$.

Another key parameter is the amount of impurity ions in the plasma. However, there is no reliable measurement of the amount of the puffed gas and no direct measurement of the total impurity amount in the plasma. Therefore, we utilized radiation power measured by two bolometer systems and particle flux measured by probes on multiple toroidal sections to determine the amount of impurity. The details are discussed in Sec. 3.2.

2.4. Configuration of the device and the measurements

Figure 1(a) is a top view of LHD with the LCFS surface, the vacuum vessel, and a pair of helical coils. We modeled a magnetic configuration with the magnetic axis at $R_{ax} = 3.6$ m and the closed helical divertors[28, 16] at every toroidal section. The modeled magnetic field is a vacuum field, and a plasma equilibrium is not taken into account. LHD has $m = 10$ periodicity, and a toroidal position is conventionally represented by a section number. Section number 1 is located at the top of Fig. 1(a) and has a horizontally elongated cross section. The section number 1.5 is located at

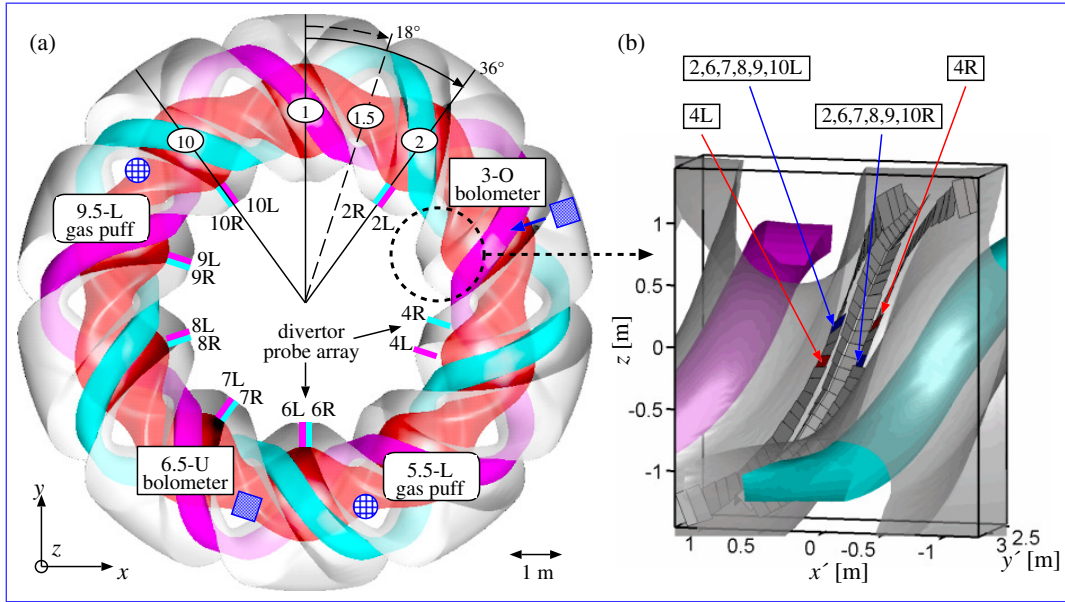


Figure 1. (a) Configuration of the puffing nozzles, the bolometer systems, and the divertor probe arrays in LHD, and (b) the relative positions of the probe arrays in a toroidal section. We note that the x' - and y' -coordinates in Fig. 1(b) are different from the x - and y -coordinates in Fig. 1(a).

an 18° shifted position in the clockwise direction and has a vertically elongated cross section. Then section number 2 has a horizontally elongated cross section again. In the following sections, we use this notation of toroidal positions for convenience.

LHD has several gas puffing nozzles. In discharges used in this work, neon gas was puffed at the lower port of the section 9.5, namely 9.5-L. Nitrogen gas was puffed at the lower port of the section 5.5, namely 5.5-L.

We used two bolometer systems at the upper port of the section 6.5, namely 6.5-U, and the outer port of the section 3, namely 3-O [29, 30, 31], as shown in Fig. 1(a). The 6.5-U bolometer is an InfraRed imaging Video Bolometer (IRVB) looking down at the plasma with a pyramid beam of sight, and we can obtain radiation information from divertor legs and X-points in a vertically elongated cross section. A cross section of the plasma viewed from the 6.5-U bolometer is given later in Fig. 12. The field of view of the 6.5-U bolometer is found in Fig. 4 in [31]. The 3-O bolometer is a resistive bolometer looking at the plasma horizontally with a wide viewing range in the toroidal direction, and we can obtain radiation information more globally. The 3-O bolometer is usually used to estimate the total radiation power.

We used a series of probe arrays on divertor plates at the inboard side of the horizontally elongated cross section as shown in Fig. 1(b). A probe array consisting of 20 probe tips aligned almost along the poloidal direction measures an ion particle flux distribution across the strike point. LHD has two series of divertor tiles in a divertor section similar to inboard and outboard divertor tiles in a tokamak device. The two series of divertor tiles are called left-side and right-side divertor tiles when viewed from

the outboard side. Two probe arrays are installed in the left-side and the right-side divertor tiles, and are called 2L and 2R at the toroidal section number 2. There are seven pairs of probe arrays at the toroidal sections 2, 4, 6, 7, 8, 9, and 10. Two probe arrays in each toroidal section locate at helically symmetric positions. The arrays 4L and 4R locate at different positions from the other arrays because of a port arrangement. Detail of the probe arrays is found in the paper[18].

3. Results and discussion

3.1. Discharge information and fundamental modeling parameters

We selected two discharges with a neon puff, #121951, and with a nitrogen puff, #123360, in the 17th LHD campaign in 2013. These discharges have a relatively long discharge time with nearly steady state electron density and electron temperature after the impurity gas puff. The duration of the neon and the nitrogen puff is 0.1 s and 0.15 s, respectively. Both discharges use the $R_{ax} = 3.6$ m configuration. The heating power of the neon-seeded and the nitrogen-seeded discharges is approximately 7 MW and 13 MW by negative-ion-based NBI, respectively. Time evolution of electron density, total radiation power, and divertor particle flux is shown in Figs. 2(a) and (b) for the neon-seeded and the nitrogen-seeded discharges, respectively. The total radiation power is measured by the bolometer at the 3-O port. We note that similar discharge conditions with different impurity seeding are preferable for comparisons, however a better combination of discharges is not available. Although we think these two discharges are sufficient to study toroidal uniformity/non-uniformity, dedicated experiments may be necessary to study differences of detailed transport characteristics such as radial and poloidal distributions of impurity ions in the plasma.

In the neon-seeded discharge, the electron density increased after the beginning of the impurity gas puff and had a maximum density after the impurity gas puff. The radiation power also had a similar time evolution. The e-folding decay time of the radiation power is approximately 2 seconds and much longer than a plasma transport time scale. The divertor particle flux decreased with a small delay from the beginning of the impurity gas puff. On the other hand, in the case of the nitrogen-seeded discharge, change of electron density and radiation power is not significant. A small flux reduction was observed but the flux recovered rapidly after the end of the impurity gas puff. A flux reduction depends on toroidal sections and is discussed in Sec. 3.3. These differences between the neon-seeded and the nitrogen-seeded discharges are typical trends in other LHD discharges.

In the modeling, firstly, we obtained a heating power and a particle source in the core due to NBI from the experimental data. Secondly, we carried out parameter scans with electron density at the core boundary at the major radius $R = 2.895$ and 4.339 m, and the cross-field transport coefficients, and we obtained best fitted coefficients with Thomson scattering measurements[32]. We note that the transport coefficients are

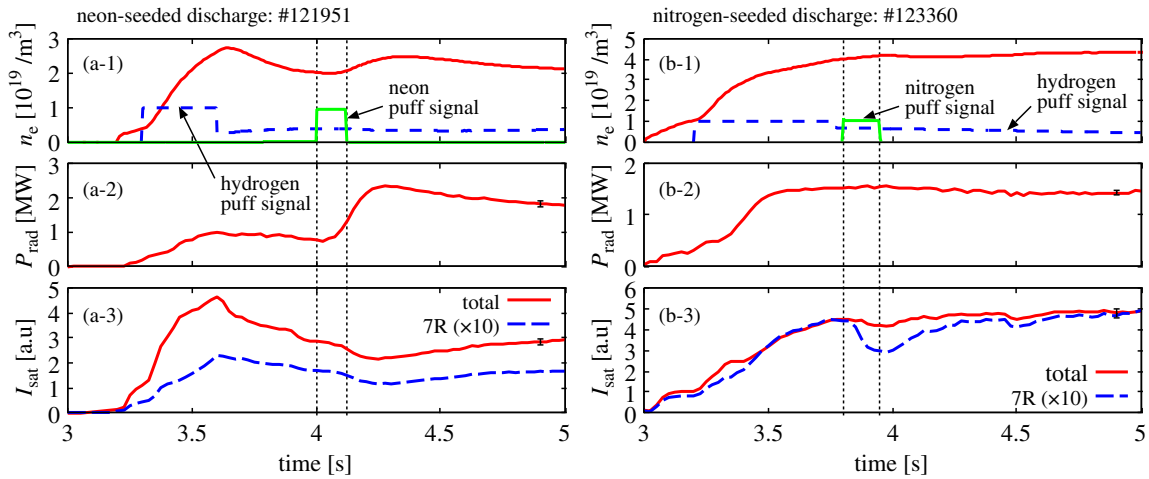


Figure 2. Time evolution of line averaged electron density, n_e , with gas puff signals, total radiation power, P_{rad} , and particle flux on divertor probe arrays, I_{sat} for (a) the neon-seeded discharge and (b) the nitrogen-seeded discharge. The particle flux of the 7R probe and the total particle flux excluding the 4R and 4L probes located at different positions from other probes are shown. The radiation power and the particle flux are averaged over a time window of 1/40 s. The black error bars at $t = 4.9$ s represent typical temporal scatters.

uniform in space, and the values are changed for the parameter scans. We performed these processes for the four cases: before/after the neon puff and before/after the nitrogen puff. Comparisons of radial distribution of electron density and temperature between Thomson scattering measurements and EMC3-EIRENE results are given in Figs. 3 and 4 for neon and nitrogen, respectively. The neon puff causes a significant increase of electron density over the entire region. On the other hand, nitrogen puff causes a subtle increase of the electron density. That trend is commonly observed in other discharges. The measured electron density with the nitrogen seeding have a drop and a peak at around $R = 2.75$ m and $R = 4.7$ m, respectively. The reason of the deviation from the EMC3-EIRENE results is unknown. However, we have good agreements except for $R = 2.75$ m and $R = 4.7$ m. The radial distribution of connection length at the same position is given in Fig. 5. The regions with long connection length, > 100 km, have monotonically varying distributions of electron temperature and density. The other regions have complicated distributions because stochastic magnetic fields cause mixing of parallel and perpendicular transport.

Four sets of particle source in the core, heating power, electron density at the core boundary, and the cross-field transport coefficients are summarized in Table 1. The influence of the particle source in the core is not significant because it is much smaller than the ionization source in the core in these cases. Another key parameter is the amount of impurity ions in the plasma and is discussed in Secs. 3.2 and 3.3.

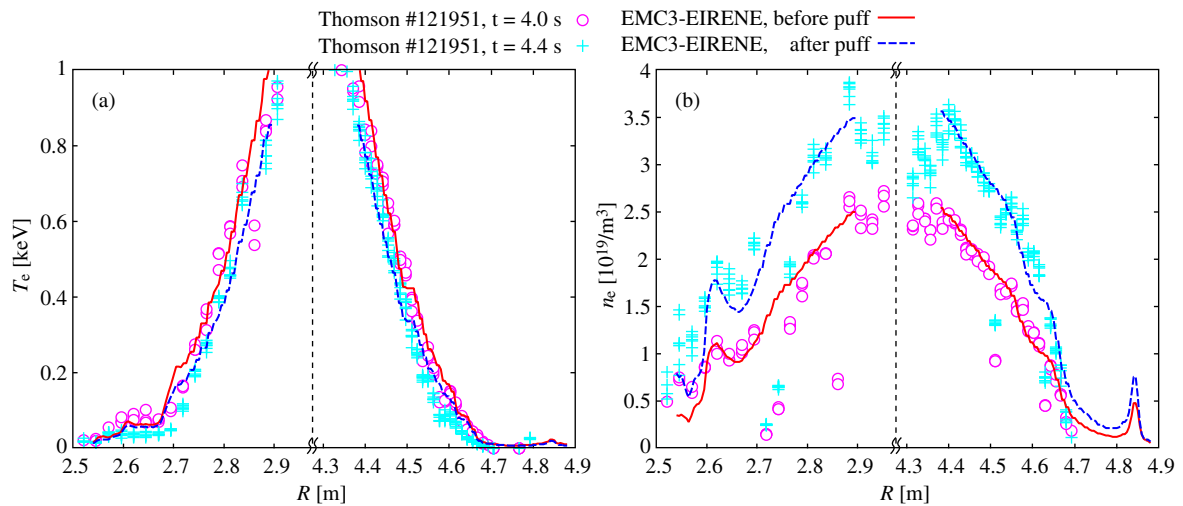


Figure 3. Electron temperature and density distributions along the mid-plane at the horizontally elongated cross section measured by Thomson scattering measurement during the neon-seeded discharge. Data points with relative errors larger than $1/4$ are excluded in Figs. 3 and 4.

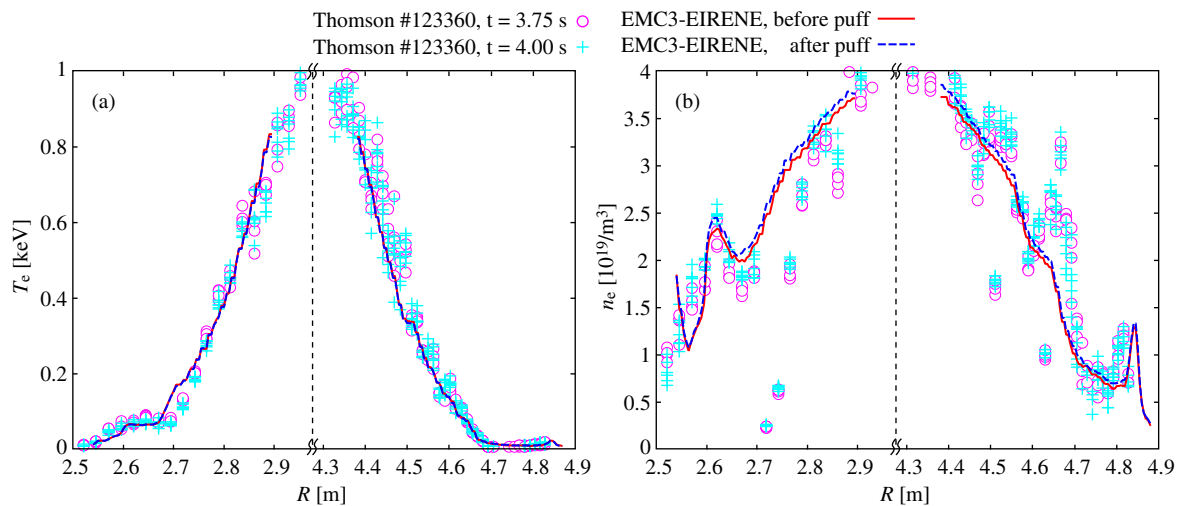


Figure 4. Electron temperature and density distributions along the mid-plane measured by Thomson scattering measurement during the nitrogen-seeded discharge.

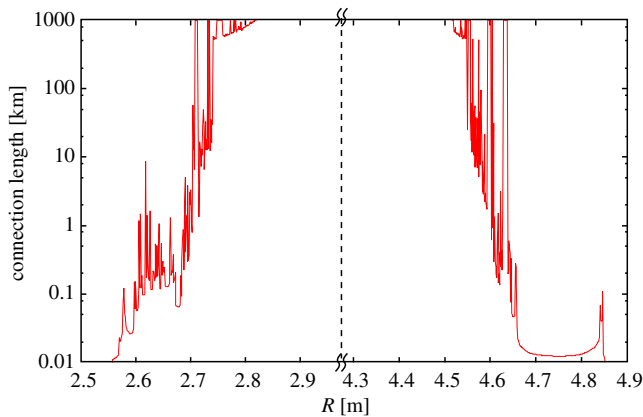


Figure 5. Connection length distribution along the mid-plane. Connection length approaches infinity near the LCFS. The LCFS positions are not clear because of stochastic fields, but are estimated at $R = 2.8$ and 4.5 m, or slightly to the core side.

Table 1. Input parameters used for the neon-seeded and the nitrogen-seeded discharges: external particle source in the core $S_{p,\text{ext}}$, external energy source in the core $S_{e,\text{ext}}$, electron density at the core boundary $n_{e,\text{core}}$, cross-field transport coefficients, D_{\perp} , $\chi_{e\perp}$, and $\chi_{i\perp}$.

	before the neon puff	after the neon puff	before the nitrogen puff	after the nitrogen puff
$S_{p,\text{ext}}$ [A]	44	49	72	74
$S_{e,\text{ext}}$ [MW]	6.8	7.5	13.0	13.2
$n_{e,\text{core}}$ [$10^{19}/\text{m}^3$]	2.5	3.5	3.7	3.8
D_{\perp} [m^2/s]	0.40	0.40	0.80	0.80
$\chi_{e\perp}, \chi_{i\perp}$ [m^2/s]	0.30	0.25	0.55	0.55

3.2. Neon seeding

The model of neon-seeded plasma uses 100% recycling of neon ions and uses an 18° calculation region with boundary conditions of the helical symmetry. The assumption of 100% recycling leads to ideal confinement of neon. In other words, there is no external source or sink except for surface recombination on the divertor plates. Therefore, there is no gas puffing nozzle in this model. An 18° calculation is numerically the same as a 360° calculation. Particle balance of impurity gas and ions is not easy to model because particle transport involves many physics with different time scales, such as ion transport, neutral transport, surface recombination, transport inside divertor plates, reflection, and absorption on the first walls. Accordingly, we used radiation power from an impurity as an input parameter in the modeling and performed a parameter scan of the radiation power with the other fixed input parameters given in Table 1. We confirmed that differences of plasma parameters between 0 MW and 3 MW nitrogen radiation are less than 5%. Therefore, adjustments of the input parameters listed in Table 1 is not necessary to investigate the influence of the radiation cooling on the particle flux. We note that a plasma can be terminated or changed significantly by an intensive impurity gas puff, as observed in experiments. However, we chose the shot number where the plasma parameters do not change drastically. In addition to these parameters, a cross-field transport coefficient of the impurity, $D_{\text{imp}\perp}$, is necessary. We performed calculations with different $D_{\text{imp}\perp}$. However, differences in results are not significant for our purpose. Therefore, we use a fixed value $D_{\text{imp}\perp} = 1 \text{ m}^2/\text{s}$ for all the cases in this work.

We use carbon as an intrinsic impurity and neon as the seeded impurity. The sputtering source model and the recycling source model mentioned in Sec. 2.2 are employed for carbon and neon, respectively. The carbon source is related to the hydrogen flux on the surface through the sputtering process by hydrogen ions with a constant sputtering yield of 2%. The neon source is determined to achieve a certain radiation power given below. The intrinsic radiation from hydrogen atoms and carbons is approximately 0.5 MW and 0.3 MW before/after the puff according to EMC3-EIRENE

results given below, respectively. The carbon radiation is approximately 0.2 MW and 0.05 MW before/after the puff, respectively. These values are consistent with the carbon radiation power reported in [33], although plasma parameters and magnetic configuration is different from the discharge used in this work. The decrease of the intrinsic radiation is caused by the reduction of electron temperature due to the significant radiation loss from neon. The radiation distribution from hydrogen, carbon, and neon are shown below in Fig. 12.

We performed a parameter scan of the radiation power from neon, $P_{\text{neon}} = 0, 1.5, 2, 3,$ and 4 MW. We obtained four results simulating corresponding measurements from the EMC3-EIRENE calculations: 1) particle fluxes on the divertor plates measured by a series of probe arrays in the seven toroidal sections, 2) a total radiation power from the whole plasma measured by the bolometer at the 3-O port, 3) an incident radiation power on the bolometer at the 6.5-U port, and 4) a two-dimensional image of the radiation measured by the bolometer at the 6.5-U port.

Figure 6 shows the toroidal distribution of the particle flux on the right and the left probe arrays with \circ marks and $+$ marks, respectively. The solid and the dashed lines are the EMC3-EIRENE results with the neon radiation of 3 MW and of 4 MW, respectively. We assume 100% recycling of neon and there is no reason to have toroidal asymmetry in the model. The flux in the figure is normalized by the flux before the puff. Therefore, the flux values represent relative changes independent of the surface area of the probes or their angles to the magnetic field. The reduction of the flux measured by the probe arrays does not have clear toroidal dependence on the puffing position at the 9.5 section. All of the flux at the right probe arrays are larger than the corresponding flux at the left probe arrays. That is typically observed in LHD, and the influence of particle drift is suggested [18, 34]. Figure 7 shows the clear trend that particle flux decreases linearly according to the radiation power. The comparison suggests that the neon radiation is approximately 4 MW. Figure 8 is a comparison of the total radiation power between the model with marks and the experiment with a line. The total radiation power includes radiation from neon, carbon, and hydrogen. The radiation from carbon and hydrogen is much less than the radiation from neon except for the result without a neon puff. The comparison suggests that the neon radiation is approximately 2 MW. Figure 9 is a comparison of the incident radiation power to the 6.5-U bolometer between the model and the experiment. We note that the incident radiation power in Fig. 9 is different from the total radiation power in Fig. 8, and it is the heat reaching at the detector through the pinhole of the bolometer. The comparison in Fig. 9 suggests that the neon radiation is approximately 4 MW. We chose 3 MW radiation from neon as the optimum input parameter determined from the above comparisons of the flux reduction and the radiation.

Figures 10 and 11 show the radiation distributions in a two-dimensional viewing area in the toroidal and the radiation directions obtained from the EMC3-EIRENE result and from the 6.5-U bolometer [35], respectively. Three regions are marked with circles in Fig. 10. The radiation regions (1) and (2) correspond to an X point trace

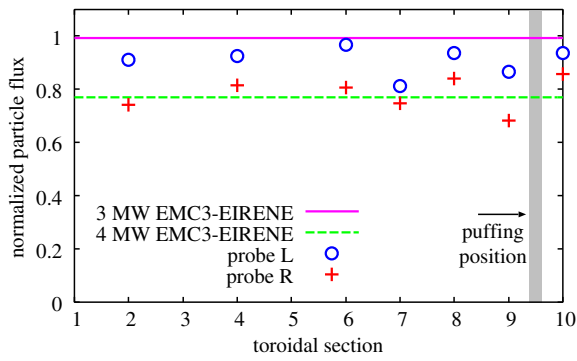


Figure 6. Toroidal flux distribution of hydrogen ions.

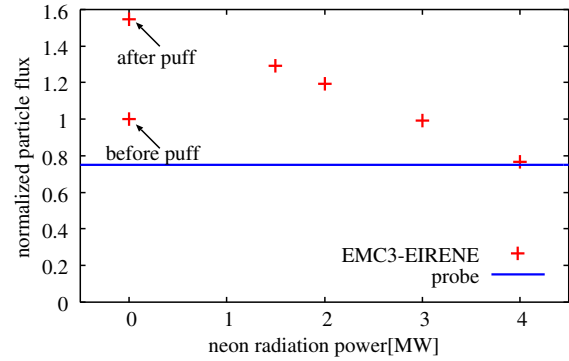


Figure 7. Total flux normalized by the flux before the neon puff.

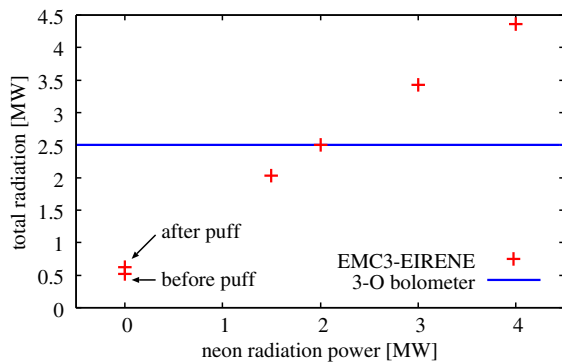


Figure 8. The total radiation power from the plasma measured at the 3-O bolometer.

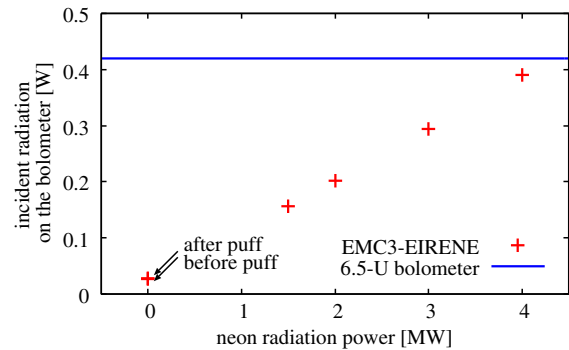


Figure 9. The radiation power reaching to the bolometer at the 6.5-U port.

of the upper divertor and the lower divertor, respectively. The region (1) includes also integration of radiation from the edge of the plasma along a line of sight. The region (3) corresponds to radiation at the edge of the plasma and has strong intensity because of integration effect along a line of sight. A similar stripe structure is observed in the experimental data in Fig. 11. The peak position at the crossing point of both of the X point traces is in good agreement. Radiation distributions of hydrogen, carbon, and neon in a cross section indicated by the white dotted line in Fig. 10 are given in Fig. 12.

3.3. Nitrogen seeding

The modeling of nitrogen-seeded plasma uses 0% recycling of nitrogen ions and uses a 360° calculation region as mentioned in Sec. 2.2. Therefore, there is no nitrogen source on the divertor plate, and neutral nitrogen atoms are released from the gas puff nozzles at the 5.5-L port. The nitrogen source is determined to achieve a certain radiation power given below. In the paper[18], 180° calculation has been performed to investigate symmetry/asymmetry characteristics near the gas puffing nozzle. However, that grid system is not sufficient to obtain the entire toroidal distribution. Therefore,

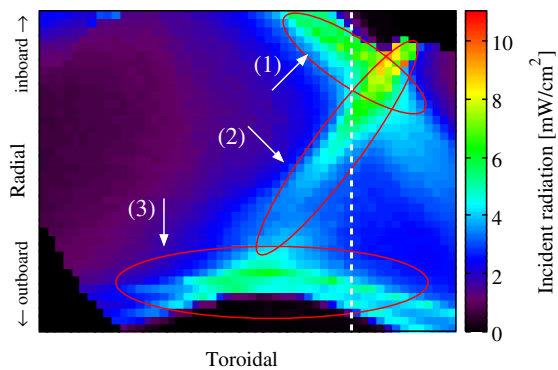


Figure 10. The synthetic image of the EMC3-EIRENE result with the neon puff. (1) and (2) are X point traces. (3) is a plasma edge region. The white dotted line shows the position of the cross section given in Fig. 12.

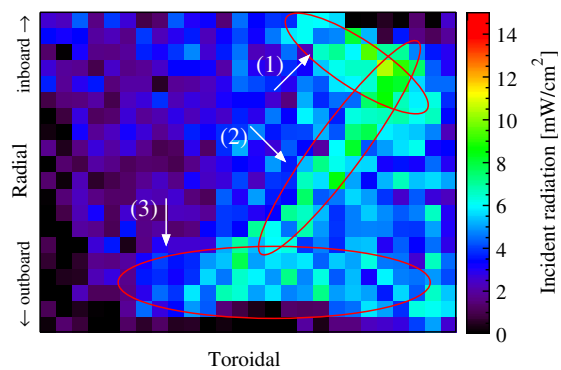


Figure 11. Two-dimensional radiation image measured by the 6.5-U bolometer with the neon puff. The red ellipses are drawn at the same positions as Fig. 10.

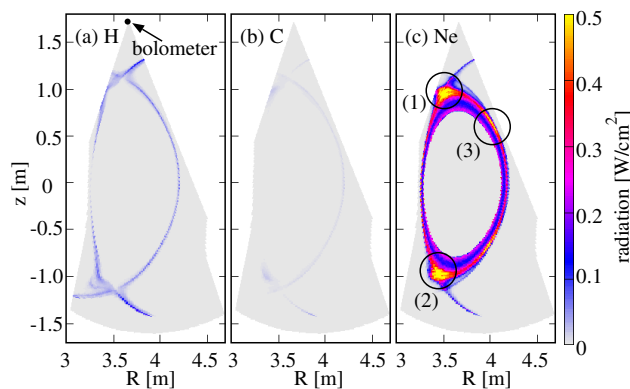


Figure 12. Radiation distribution of (a) hydrogen, (b) carbon, and (c) neon in the cross section indicated in Fig. 10. The regions (1), (2), and (3) correspond to the region numbers in Fig. 10. The gray hatched area is the visible region of the bolometer.

we have developed the 360° grid system. Before a 360° calculation, we performed an 18° calculation with carbon and nitrogen impurities, and confirmed that carbon radiation was much smaller than nitrogen radiation. Therefore, we used only nitrogen impurity to reduce a computational cost. We performed 18° calculations to determine input parameters summarized in Table 1. A parameter scan of the radiation power is necessary to determine the radiation power from nitrogen. However, a 360° calculation requires too much memory and time. Therefore, we chose 3 MW radiation from nitrogen from a parameter scan with 18° calculations to find similar reduction of a particle flux on the divertor probes to the experiment. We obtained the toroidal flux distribution on the divertor tiles and compared the flux normalized by the flux before the puff with the probe measurement in Fig. 13. In both the modeling and the experiment, a flux reduction is clearly observed only at larger/smaller toroidal section numbers than the section number of the puffing position for the right/left divertor tiles, respectively. The different trend of the R/L divertor fluxes is closely connected to impurity transport along magnetic field lines. As discussed in the preceding work[18], flux tubes passing through

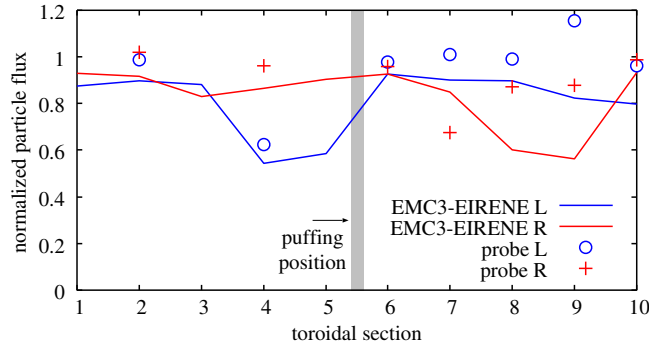


Figure 13. Toroidal flux distribution of hydrogen ions.

the impurity gas localized at the toroidal section 5.5 carry impurity ions and suffer from large radiation loss and hence have a reduction of particle flux. This reduction process arises from the local impurity source and supports the assumption of low recycling coefficient of nitrogen. However, there is a deviation that the model has a reduction at the sections 8R and 9R, but the experiment has a reduction at the section 7R.

The reason for the toroidal shift of the reduction regions is not clear from the modeling here. However, several possible reasons may be listed: gas flow from the nozzle, particle drifts, the magnetic field structure, the reflection coefficient of the nitrogen neutrals, and the recycling coefficient of the nitrogen ions.

- The gas puffing nozzle is located at the 5.5-U port and is far from the plasma surface. Therefore, we assume that the gas flow expands in the duct of the port. We set many point sources of neutral particles in order to cover the port. However, the calculation region has a restriction due to the grid construction and the point sources are near the plasma and divertor plates. The difference of the nitrogen gas flow could cause different ionization distribution.
- Cross-field particle transport such as grad-B, curvature, and $E \times B$ drifts could cause different transport as observed in the R/L asymmetry in the divertor particle flux in Fig. 6. Influence on impurity ion transport might be different from the influence on hydrogen ion transport.
- The magnetic field in our model is vacuum magnetic field and is different from the actual magnetic field modulated by the plasma. The difference is not large, but it causes a different magnetic field structure. In experiments, different flux distribution on the divertor plates are observed in the case of relatively high β plasmas[34].
- We use 100% reflection of the impurity neutrals on surfaces. Smaller reflection coefficient could cause shrinking of the region with a flux reduction. However, the small reflection coefficient might not cause the shift of the region observed here.
- A larger recycling coefficient will cause wider radiation and a wider flux reduction. These are opposite changes and might not be the reason for the toroidal shift.

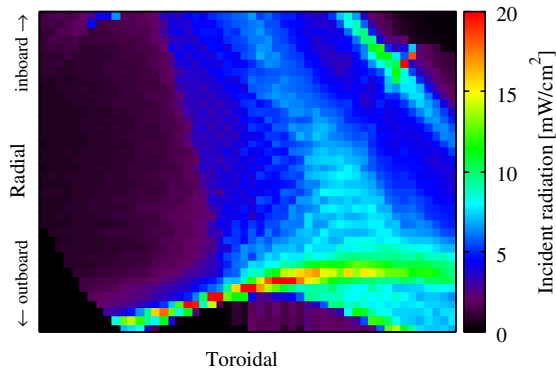


Figure 14. Synthetic image of the EMC3-EIRENE result with the nitrogen puff.

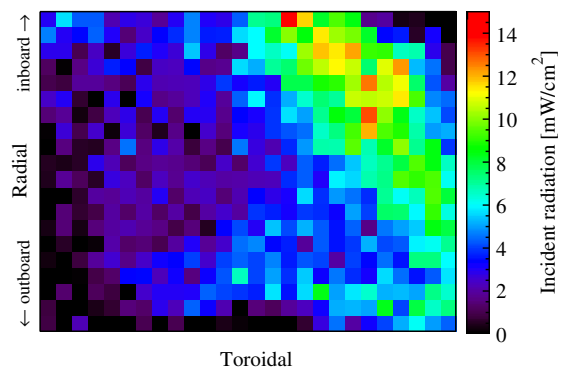


Figure 15. Two-dimensional radiation image measured by the 6.5-U bolometer with the nitrogen puff.

Comparison of the two-dimensional radiation distributions viewed from 6.5-U port is given in Figs. 14 and 15 obtained from the EMC3-EIRENE result and from the 6.5-U bolometer, respectively. Both images have two stripes for the upper X point trace and the plasma edge. However, the relative intensities of the two stripes are opposite. The result of the model has very strong radiation in the plasma edge, but the experiment has weak radiation in the plasma edge. Also, the total radiation power reaching the bolometer in the model is approximately twice the power as in the experiment. That finding suggests that the nitrogen radiation power in the model should be one-half of the present model. However, that is not obvious because the different radiation stripes mean different nitrogen transport or a different source distribution in the model. The uncertainties listed above should be clarified.

4. Conclusions

Modeling of impurity-seeded plasma in LHD has been conducted with the three-dimensional transport code EMC3-EIRENE. High and low recycling coefficients for impurity ions are assumed to include low and high absorption rates on surfaces due to low and high chemical activity of neon and nitrogen, respectively. We used the radial distributions of electron density and electron temperature obtained by the Thomson scattering measurement to determine the electron density at the core boundary and the cross-field transport coefficients of particle and energy. We also used probe arrays on the divertor plates in seven toroidal sections and two bolometer systems at 3-O port and 6.5-U port in order to determine the radiation power from impurities.

From the comparisons of the ion particle flux on the divertor plates, the model reproduced the toroidal uniformity and the non-uniformity of the flux reduction due to radiation loss from neon and nitrogen, respectively. The flux reduction takes place at the position with the lower toroidal section number than the puffing section for the right-side divertor and at the higher toroidal section number for the left-side divertor in

both the model and the experiment. Therefore, we conclude that the most prominent difference in impurity transport can be modeled by high and low recycling coefficient of impurity arising from low and high chemical activity, respectively. However, there is a toroidal shift of the position in the flux reduction for the right-side divertor. The reason is an open question. Physical processes such as gas flow from the nozzle, particle drifts, the magnetic field structure, the reflection coefficient of the nitrogen neutrals, and the recycling coefficient of the nitrogen ions should be investigated. Physical process with regard to the flux reduction caused by radiation cooling also should be clarified in a future study.

From the parameter scan of the neon radiation power, we chose 3 MW radiation as an input parameter of the model and obtained a similar particle flux reduction and radiation power with the experimental results of the probe measurements and bolometer measurements, respectively. The two-dimensional radiation distribution viewed from the 6.5-U port agreed with the bolometer measurements especially with regard to three clear stripes of radiation in the case of neon seeding. However, the two-dimensional radiation distribution in the case of nitrogen seeding has a significant difference from the measurement. Both the model and the experiment have two stripes but the relative intensities of these stripes were opposite. That suggests different impurity transport or different impurity source distribution. In addition to the different physical processes mentioned above, a sensitivity study of heating power or electron density is required to understand the influence of the force acting on impurity ions.

Acknowledgments

This work was supported partly by JSPS KAKENHI Grant Number 16K18340, 16H06139, [16H02440](#) and 15H04236 and performed under the auspices of the NIFS Collaboration Research program (NIFS16KNST100, NIFS15KLPP040) and Numerical Simulation Reactor Research Project (NIFS11UNTT004).

References

- [1] Asakura N *et al* 2017 *Nucl. Fusion* **57** 126050.
- [2] Hoshino K *et al* 2017 *Plasma Fusion Res.* **12** 1405023.
- [3] Brezinsek S *et al* 2017 *Nucl. Fusion* **57** 116041.
- [4] Homma Y *et al* 2017 *Nucl. Mater. Energy* **12** 323.
- [5] Kallenbach A *et al* 2013 *Plasma Phys. Contr. Fusion* **55** 124041.
- [6] Lunt T *et al* 2014 *Plasma Phys. Contr. Fusion* **56** 035009.
- [7] Hoshino K *et al* 2012 *Contrib. Plasma Phys.* **52** 550.
- [8] Feng Y *et al* 2017 *Plasma Phys. Contr. Fusion* **59** 034006.
- [9] Feng Y *et al* 2014 *Contrib. Plasma Phys.* **54** 426.
- [10] Feng Y *et al* 2004 *Contrib. Plasma Phys.* **44** 57.
- [11] Reiter D *et al* 2005 *Nucl. Fusion* **47** 172.
- [12] Oyabu N *et al* 1994 *Nucl. Fusion* **34** 387.
- [13] Kobayashi M *et al* 2015 *Nucl. Fusion* **55** 104021.
- [14] Kawamura G *et al* 2014 *Contrib. Plasma Phys.* **54** 437.

- [15] Dai S *et al* 2016 *Nucl. Fusion* **56** 066005.
- [16] Masuzaki S *et al* 2013 *J. Nucl. Mater.* **438** S133-S138.
- [17] Morisaki T *et al* 2015 *J. Nucl. Mater.* **463** 640-643.
- [18] Tanaka H *et al* 2017 *Nucl. Mater. Energy* **12** 241.
- [19] Dai S *et al* 2017 *Plasma Phys. Contr. Fusion* **59** 085013.
- [20] OPEN-ADAS <http://open.adas.ac.uk/>.
- [21] Eckstein W and Heifetz D B 1986 *MPI-Garching Report* IPP 9/59.
- [22] Bateman G 1980 *PPPL Appl. Phys. Rep.* No. 1.
- [23] Rubel M *et al* 2011 *J. Nucl. Mater.* **415** 5223.
- [24] Tokitani M *et al* 2005 *Nuclear Fusion* **45** 1544.
- [25] Grigull S *et al* 1999 *J. Nucl. Mater.* **275** 158.
- [26] Kallenbach A *et al* 2010 *Plasma Phys. Contr. Fusion* **52** 055002.
- [27] McCracken G M *et al* 1981 *Phys. Plasma* **4** 1681.
- [28] Morisaki T *et al* 2013 *Nuclear Fusion* **53** 063014.
- [29] Peterson B J *et al* 2003 *Plasma Phys. Contr. Fusion* **45** 1167.
- [30] Pandya S N *et al* 2014 *Rev. Sci. Instrum.* **85** 073107.
- [31] Mukai K *et al* 2014 *Plasma Fusion Res.* **9** 3402037.
- [32] Yamada I *et al* 2016 *Rev. Sci. Instrum.* **87** 11E531.
- [33] Zhang H *et al* 2016 *Plasma Fusion Res.* **11** 2402019.
- [34] Masuzaki S *et al* 2006 *Fusion Sci. Technol.* **50** 361.
- [35] Mukai K *et al* 2015 *Nuclear Fusion* **55** 083016.